Supporting Information

for

Operando monitoring of gas bubble evolution in water electrolysis by single high-frequency impedance

Kamran Dastafkan[1], Shuhao Wang,[1,2] Shuang Song,[3] Quentin Meyer,[1] Qiang Zhang,[2] Yansong Shen,[3] Chuan Zhao*,[1]

[1] School of Chemistry, The University of New South Wales, Sydney, New South Wales, 2052, Australia. Email: chuan.zhao@unsw.edu.au

[2] Beijing Key Laboratory of Green Chemical Reaction Engineering and Technology, Department of Chemical Engineering, Tsinghua University, Beijing 100084, China.

[3] School of Chemical Engineering, University of New South Wales, Sydney, NSW 2052, Australia

Physical characterizations

Scanning electron microscopy (SEM), and energy dispersive X-ray spectrometry (EDS) were performed using a Joel 7001 microscope. Transmission electron microscopy (TEM) with high resolution (HRTEM) were conducted by a JEOL JEM-F200 Multi-Purpose FEG-S/TEM operating at an accelerating voltage of 200 kV. An optical microscope (Nikon SMZ25, Japan) was used for operando gas bubble evolution analysis. Underwater and under-electrolyte adhesion force measurement was conducted using a microelectromechanical balance system (Dataphysics DCAT21, Germany), respectively.

Fast Fourier transform (FFT) simulation

Dynamic resistance variation is processed in terms of frequency distribution using a discrete (fft) function tool in MATLAB®. The characteristic frequency amplitude peaks as a function of frequency domain, contained within the recorded resistance signal, are extracted and de-noised with a 4th order Savitzky–Golay filter using sgolayfilt function in MATLAB®[1].

```
X=[]; %raw temporal data in X

%f are the points omitted at the beginning of the experiment (activation of
electrode)
Fs = 0.5;            % Sampling frequency
T= 1/Fs;             % Sampling period
L= length(X);             % Length of signal
t= (0:L-1)*T;        % Time vector

Y= fft(X);
%Compute the two-sided spectrum P2. Then compute the single-sided spectrum P1
based on P2 and the even-valued signal length L.

P2 = abs(Y/L);
P1 = P2(1:L/2+1);
P1(2:end-1) = 2*P1(2:end-1);
c=0.15;
d=0.01;
u=6;
v=151;
e=10;
```

```
[a,b]=envelope(P1,e,'peak');                    %e is by how many points the
peaks are averaged (10 is a good value)
f = Fs*(0:(L/2))/L;
B = sgolayfilt(P1,u,v);
figure(3)
plot(f,P1,f,B,f,a,f,b)
title('FFT')
xlabel('f (Hz)')
ylabel('|P1(f)|')
ylim([0 d])
xlim([0.0 c])

k=[f' P1 B a b];
X=[]; %raw temporal data in X

%f are the points omitted at the beginning of the experiment (activation of
electrode)
Fs = 0.5;            % Sampling frequency
T= 1/Fs;             % Sampling period
L= length(X);             % Length of signal
t= (0:L-1)*T;        % Time vector


Y= fft(X);
%Compute the two-sided spectrum P2. Then compute the single-sided spectrum P1
based on P2 and the even-valued signal length L.

P2 = abs(Y/L);
P1 = P2(1:L/2+1);
P1(2:end-1) = 2*P1(2:end-1);
c=0.15;
d=0.01;
u=6;
v=151;
e=10;

[a,b]=envelope(P1,e,'peak');  %e is by how many points the peaks are averaged
(10 is a good value)
f = Fs*(0:(L/2))/L;
B = sgolayfilt(P1,u,v);
figure(3)
plot(f,P1,f,B,f,a,f,b)
title('Output Name')
xlabel('f (Hz)')
ylabel('|P1(f)|')
ylim([0 d])
xlim([0.0 c])

k=[f' P1 B a b];
```

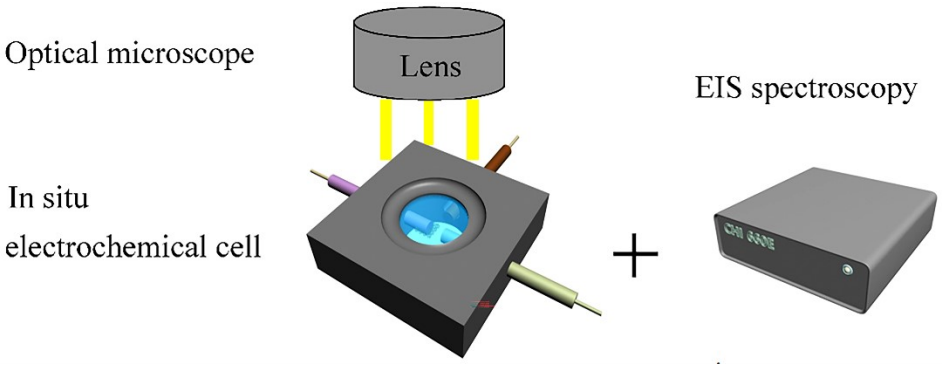

Figure S1. Schematic representation of the *operando* optical microscopy.

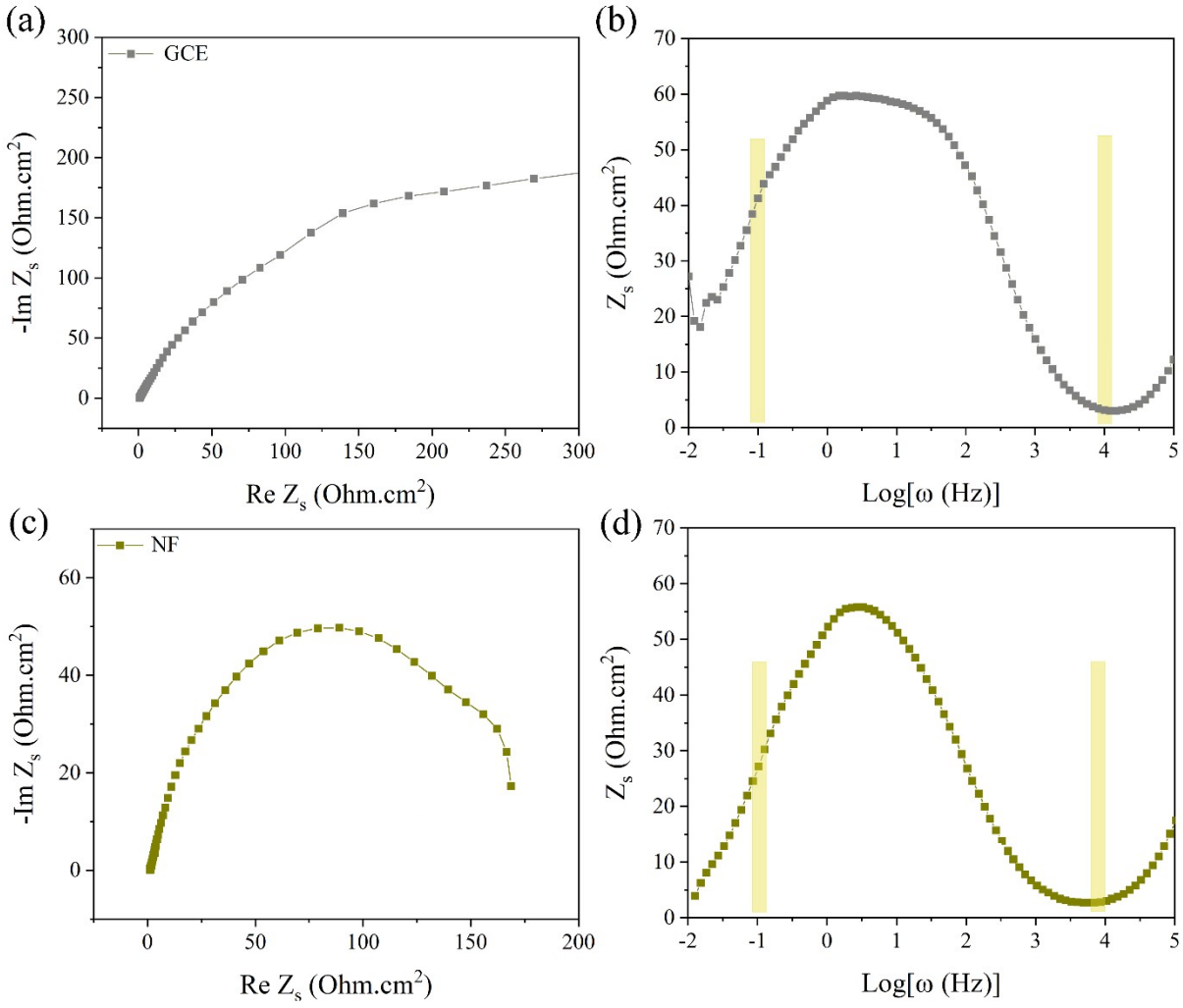

Figure S2. Left: Nyquist and right: Bode-phase plots obtained over (a) and (b) GCE at -1.45 V, and over (c) and (d) NF at -0.15 V (V vs RHE).

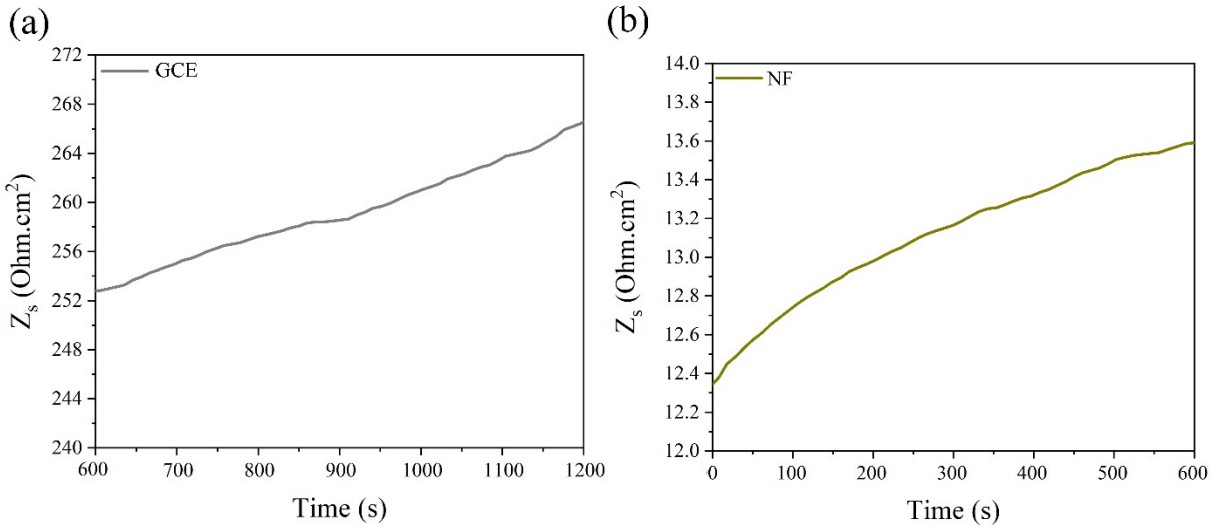

Figure S3. *Operando* dynamic resistance variation recorded at a low frequency of 0.1 Hz on (a) GCE at -1.45 V and (b) NF at -0.15 V (V vs RHE).

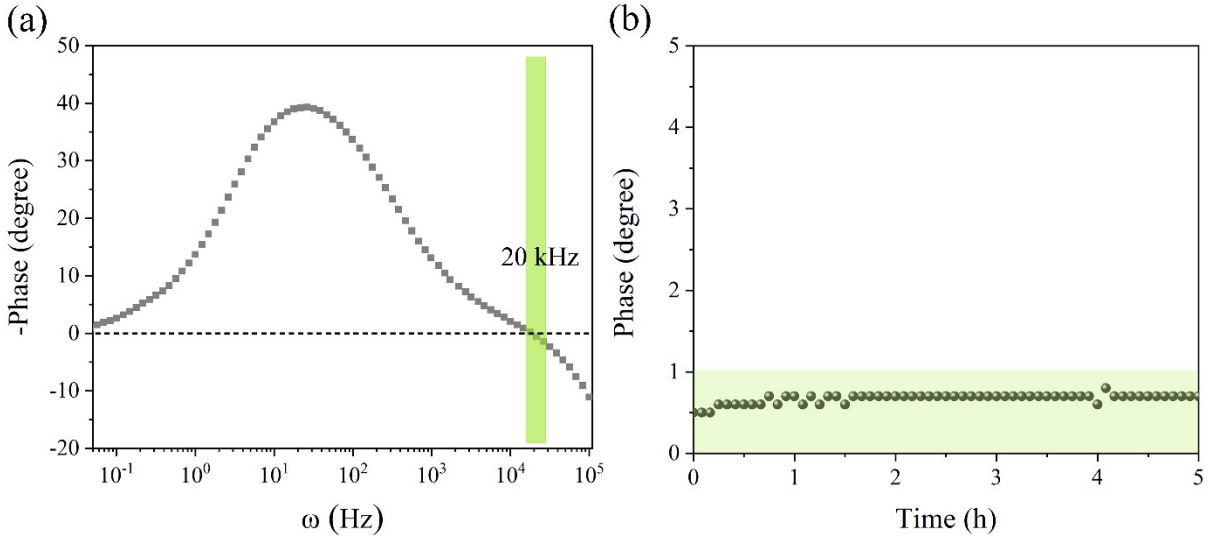

Figure S4. Bode-phase plot and dynamic phase variation of bare NF at -100 mA cm^{-2}.

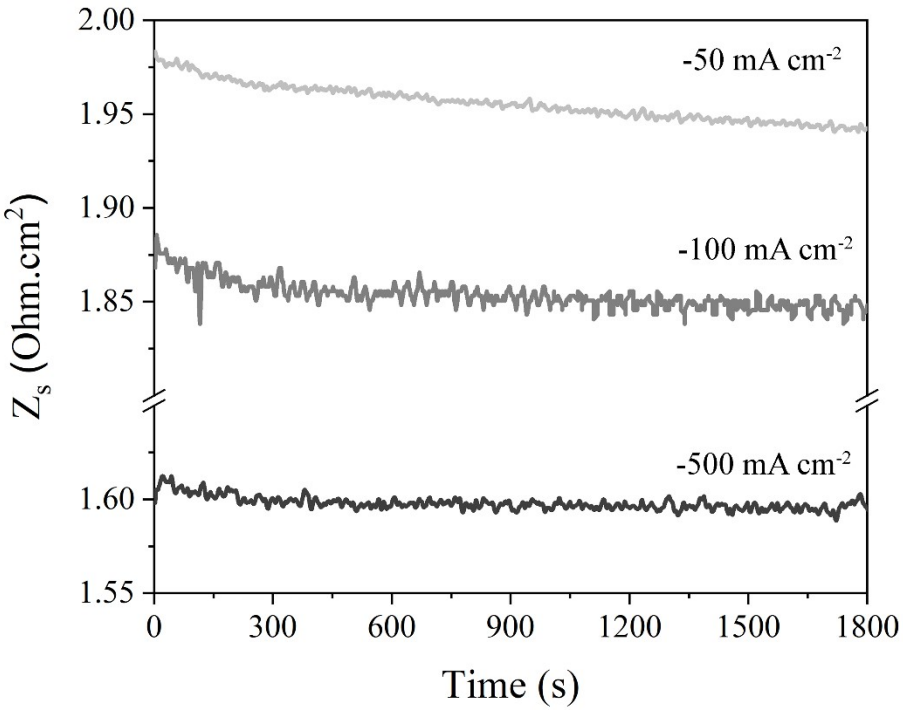

Figure S5. Dynamic resistance variation recorded on bare NF electrode (0.25 cm^2) in standard three-electrode electrochemical cell at 20 kHz at fixed current densities of -50, -100, and -500 mA cm^{-2}.

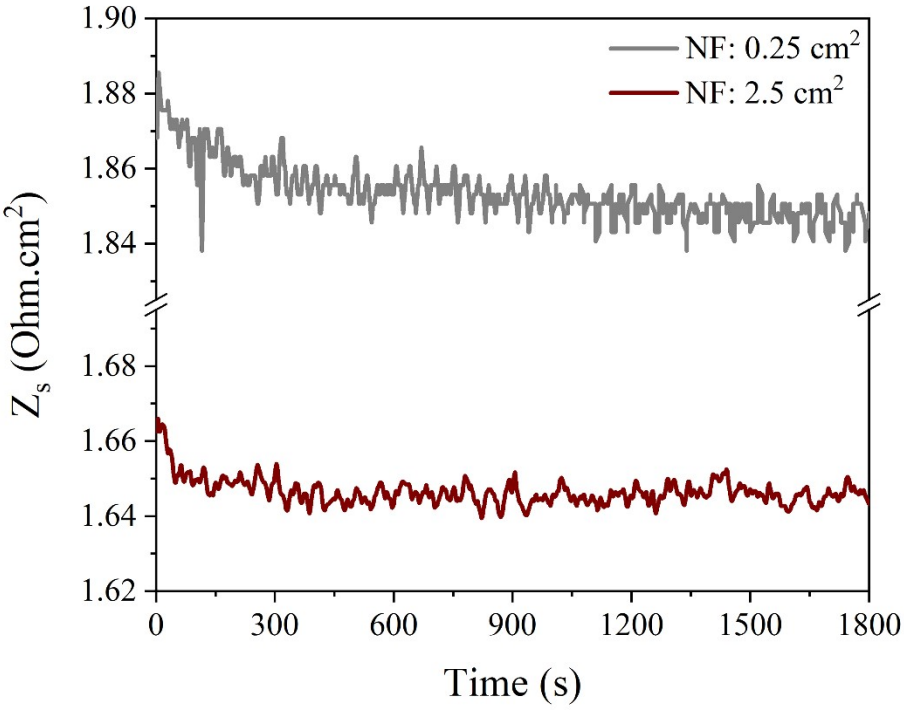

Figure S6. Dynamic resistance variation recorded on bare NF electrode in standard three-electrode electrochemical cell with geometric sizes of 0.25 and 2.5 cm^2 at 20 kHz and a current density of -100 mA cm^{-2}.

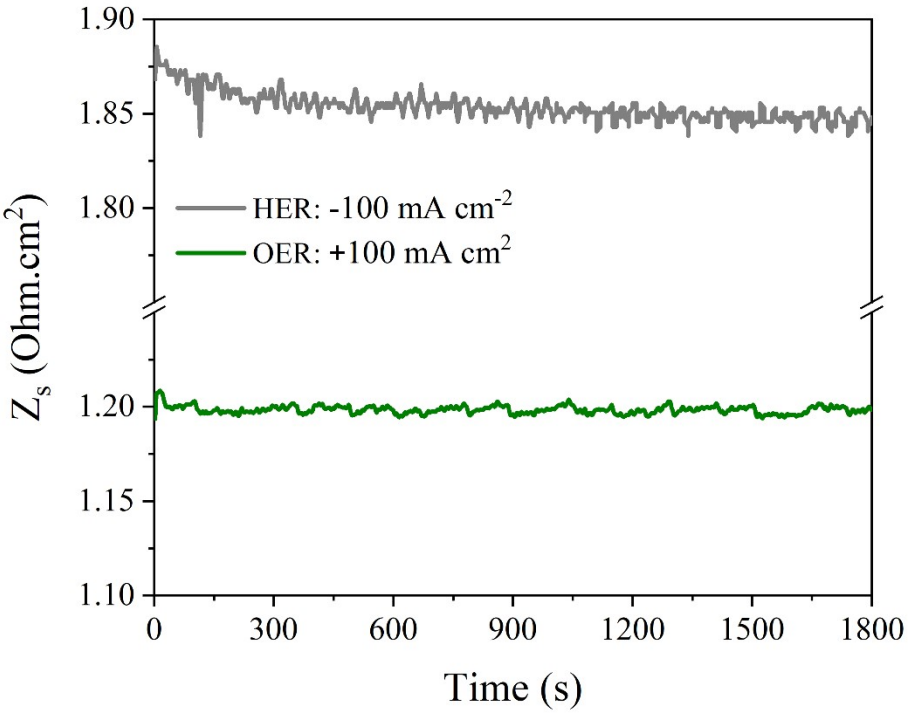

Figure S7. Dynamic resistance variation recorded on bare NF electrode (0.25 cm^2) in standard three-electrode electrochemical cell at 20 kHz and current densities of -100 and 100 mA cm^{-2} for HER and OER.

Supplementary Note 1

The alkaline HER (1M KOH) performance attained by $Ni(OH)_2$@N-NiC/NF depicts significantly reduced overpotentials at low and high potential regions compared with NF and $Ni(OH)_2$/NF (**Figure 2a**). Specifically, a low overpotential of 267 mV is obtained to deliver a moderate current density of -100 mA cm^{-2} in HER polarization without any ohmic resistance compensation, which is 113 mV smaller than that attained by monophasic $Ni(OH)_2$/NF nanosheets[2]. Also, at a large applied potential of -0.5 V vs RHE, $Ni(OH)_2$@N-NiC/NF electrode delivers more than 500 mA cm^{-2}, whereas the monophasic $Ni(OH)_2$/NF electrode shows 200 mA cm^{-2}.

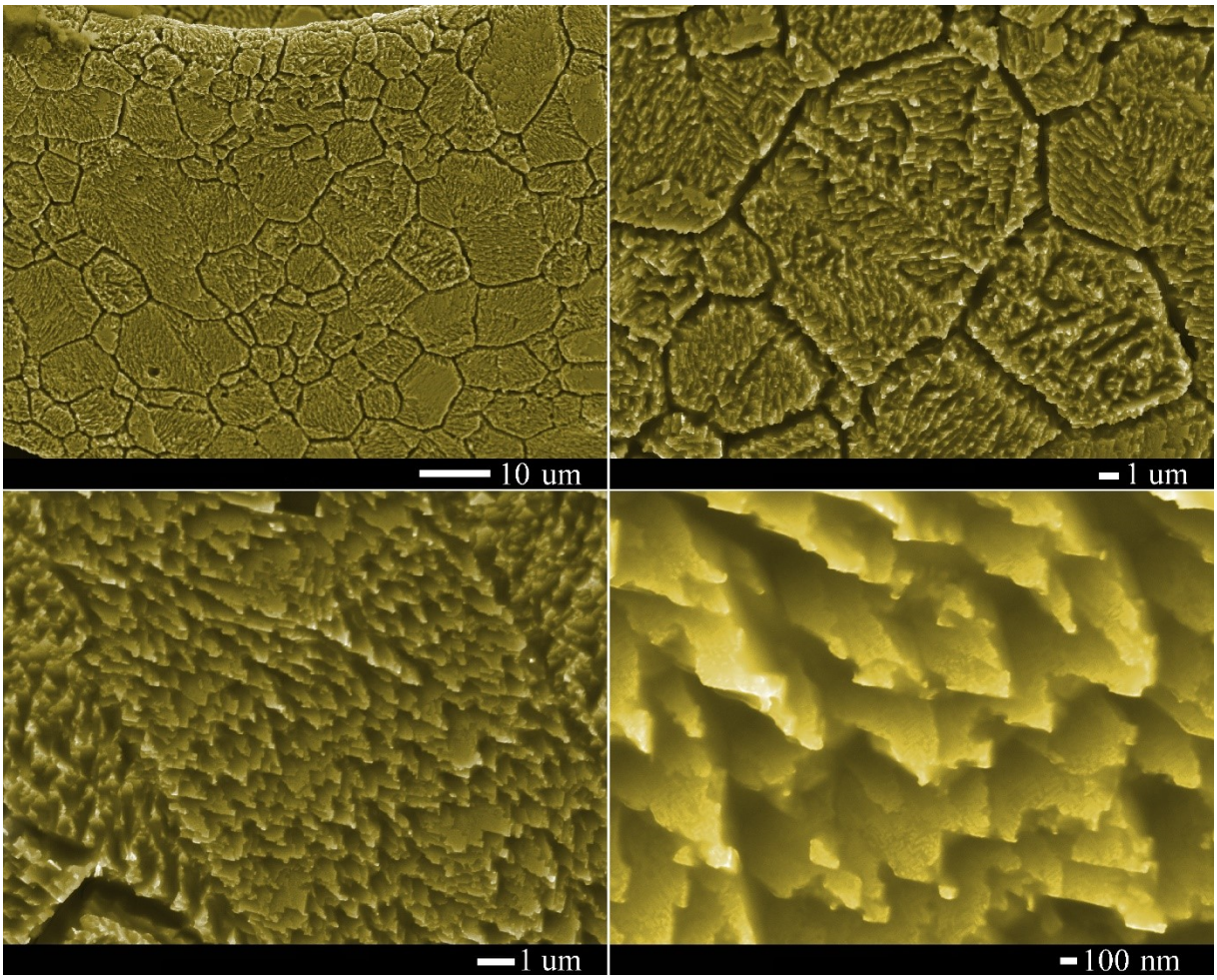

Figure S8. SEM images of $Ni(OH)_2$@N-NiC/NF at various magnifications.

Supplementary Note 2

An initial Cassie-Baxter state is a wetting state on non-ideal rough and heterogeneous surface with gas pockets and a Young contact angle between 90° to 180°)[3], which is considered for a triple phase boundary of an electrode surface, electrolyte, as well as air pockets within the porous surface structure. The Wenzel state is a wetting state on non-ideal rough surfaces with an apparent liquid contact angle)[3]. Generally, the faster wetting transition to Wenzel state on electrodes during gas evolving reactions, the higher surface wettability by electrolyte and faster gas bubble dissipation.

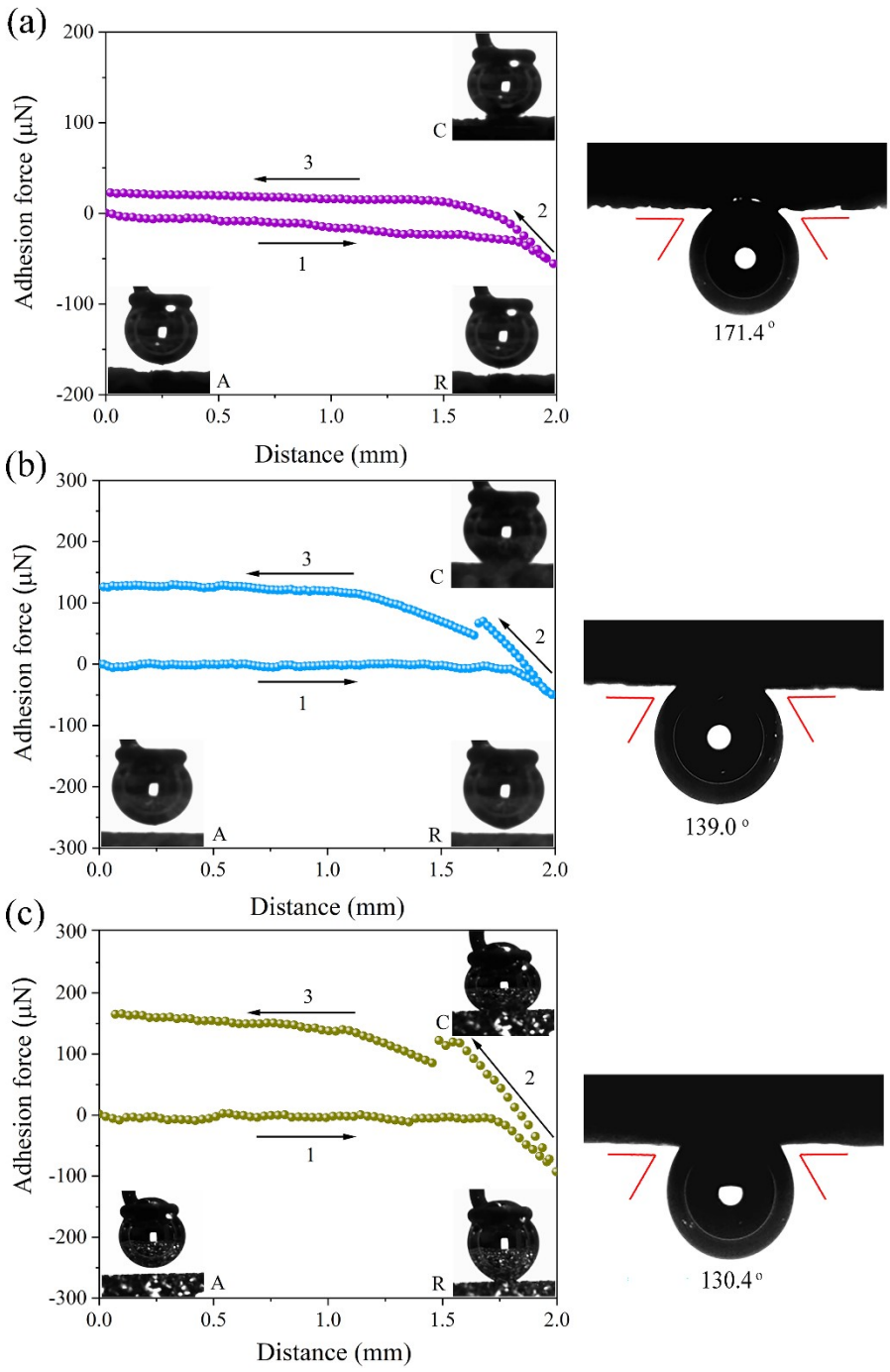

Figure S9. Left: adhesion force and right: underwater gas bubble contact angle measurements on (a) $Ni(OH)_2$@N-NiC/NF, (b)) $Ni(OH)_2$/NF, and (c) bare NF. Insets: snapshots of the introducing air gas bubble during advancing, contact, and receding processes.

Supplementary Note 3

The growth and release of a single hydrogen bubble is modelled at different time intervals over three types of surface morphology: flat surface, nanosheets, and multi-directional surface hierarchies. An upward bubble transport is followed by buoyancy force through Y direction. At the time step of 0, the calculated bubble diameters are 17.0, 11.5 and 10.2 (LB unit), respectively on the flat surface, nanosheets, and hierarchies. Then, a significantly higher velocity and less adhesion is observed for the dissipating gas bubble over the hierarchies (**Figure S10**). The interactions among a population of gas bubbles of various size could impact the velocity, but this effect governs all three morphologies. Hence, the simulated GBE is carried through at large current densities.

The sluggish nucleation, growth, and detachment of a single hydrogen bubble on the flat surface of NF skeleton is exacerbated by its slow transport through the 3D framework. Thus, NF surface is constantly blocked by the onsite gas bubble. $Ni(OH)_2$ micro and nanosheets as catalysts weakly mitigate the surface adhesion force. Only multi-directional surface hierarchies allow the formation of a smaller gas bubble and minimum surface adhesion for a fast release (**Figure S11a**). The simulated dynamic gas bubble growth and release from XZ-plane depict higher slopes in both trends for the surface hierarchies than nanosheets, while the plane surface illustrates no change over time (**Figure S11b** and **c**). Herein, surface hierarchies with different orientations not only minimize the surface energy to boost GBE dynamics (smaller size and rapid detachment), but also provide through-porous space that accelerate the upward bubble transport driven by buoyancy. This allows the superior performance of $Ni(OH)_2$@N-NiC/NF at large current densities.

(a)

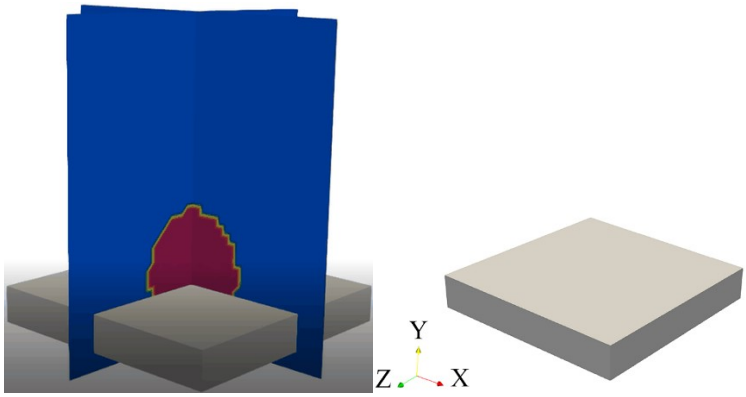

(b)

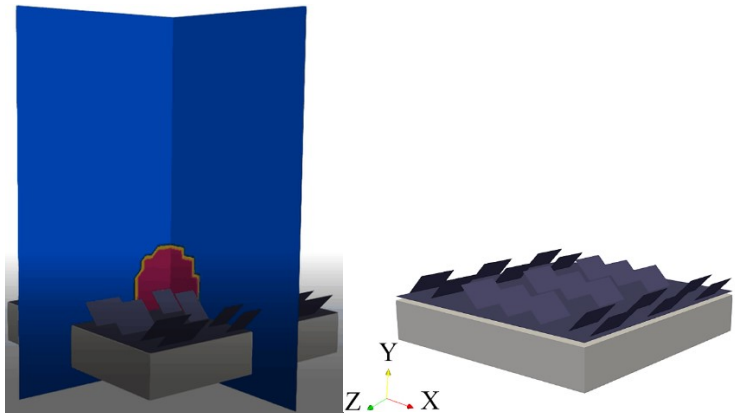

(c)

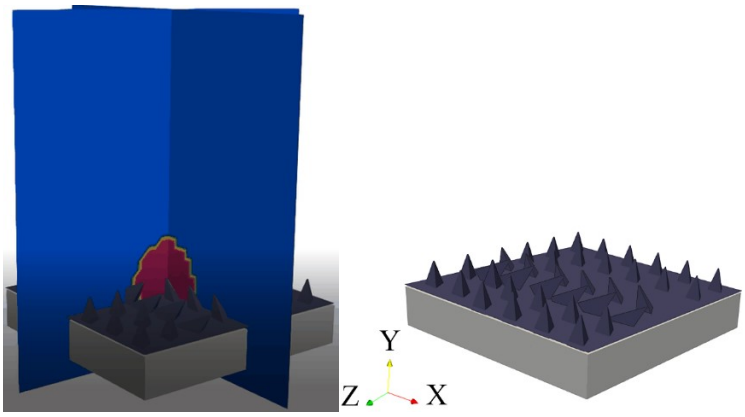

Figure S10. Multimedia representation of GBE velocity and gas bubble detachment from the (a) flat surface of bare NF, (b) nanosheets over $Ni(OH)_2$/NF, and (c) multi-directional surface hierarchies of $Ni(OH)_2$@N-NiC/NF.

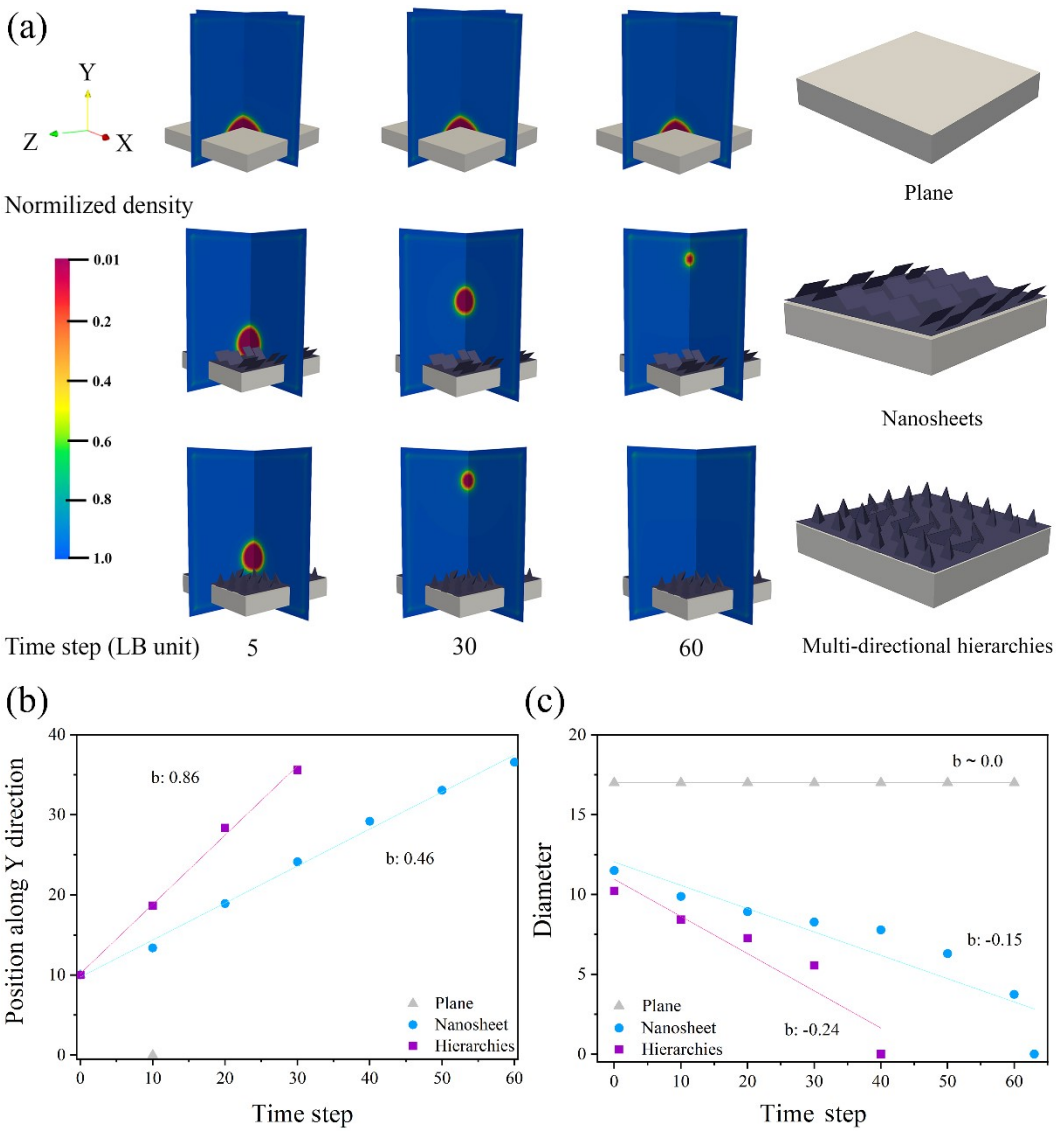

Figure S11. (a) LBM illustration of single hydrogen GBE at three surface morphologies. Quantitative bubble (b) release and (c) size simulation as a function of time step. LB unit is applied for the parameters.

Figure S12. Schematic representation of the *operando* optical microscopy of gas bubbles using a home-made three-electrode electrochemical cell with a transparent window.

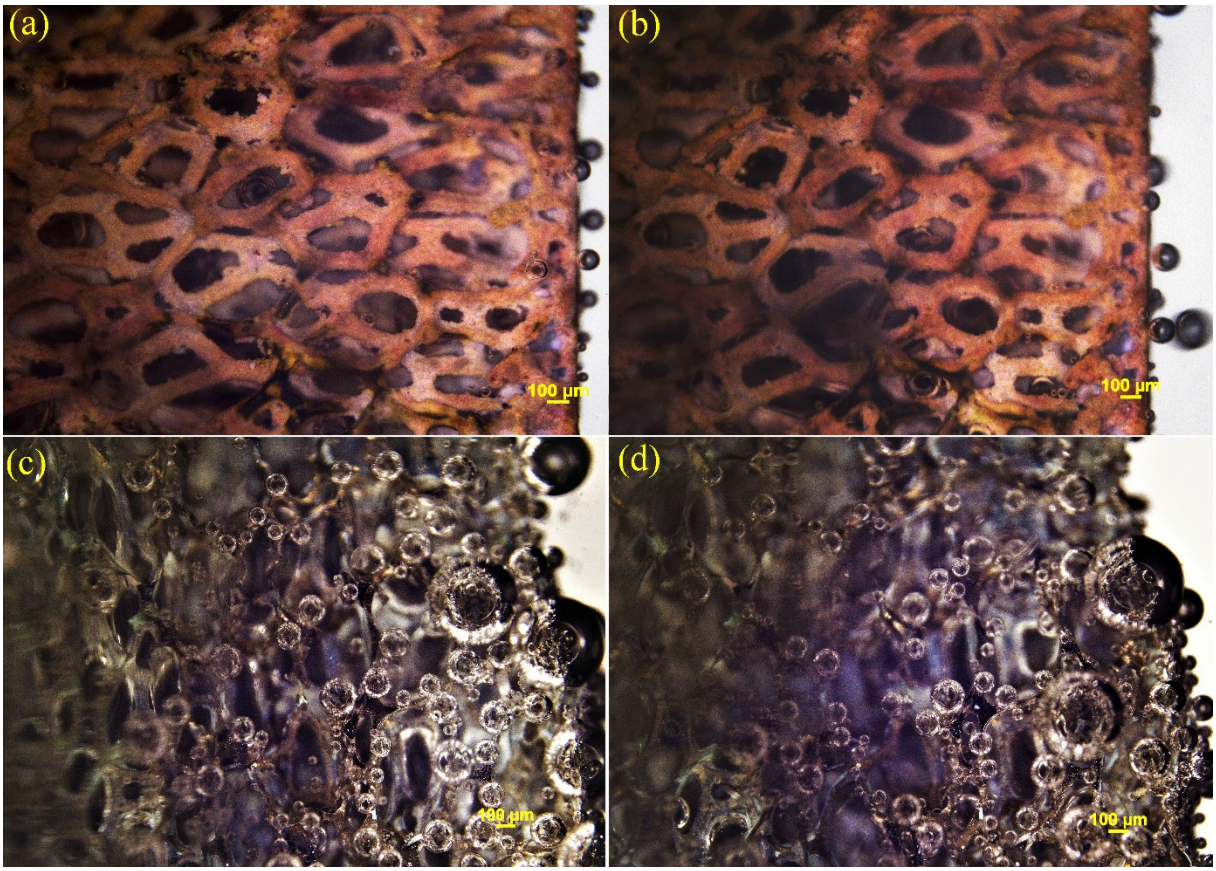

Figure S13. Optical microscopic images of evolving hydrogen gas bubbles over top: $Ni(OH)_2$@N-NiC/NF and bottom: $Ni(OH)_2$/NF at potentials of (a, c) 0.345 and (b, d) 0.445 V vs RHE.

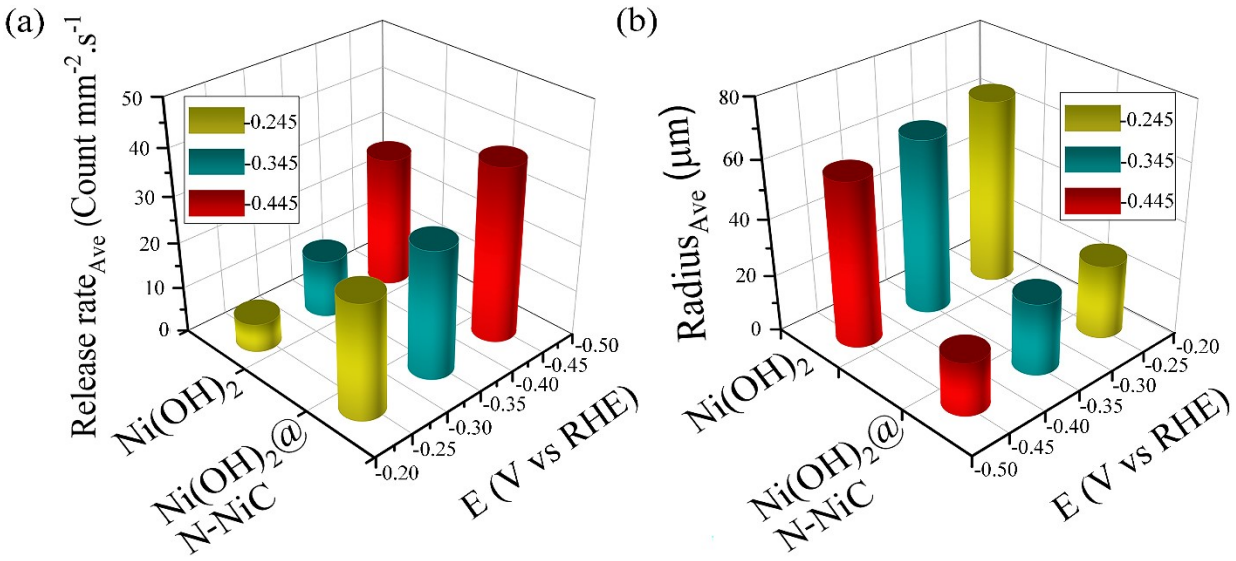

Figure S14. The trends of average (a) release rate and (b) gas bubble radius over $Ni(OH)_2$@N-NiC/NF and (c) $Ni(OH)_2$/NF within a period of 60 s at different potentials.

Supplementary Note 4

The distinctively different release rate in the 3D surface plots at different time intervals and potentials suggests that the hierarchies in different orientation zones at the surface of $Ni(OH)_2$@N-NiC/NF allocate more gas bubble flow with the same direction of buoyancy force and facilitate a through-plane bubble transport. Instead, gas bubbles experience an in-plane transport over $Ni(OH)_2$/NF and the major driving force for GBE is increasing the energy input.

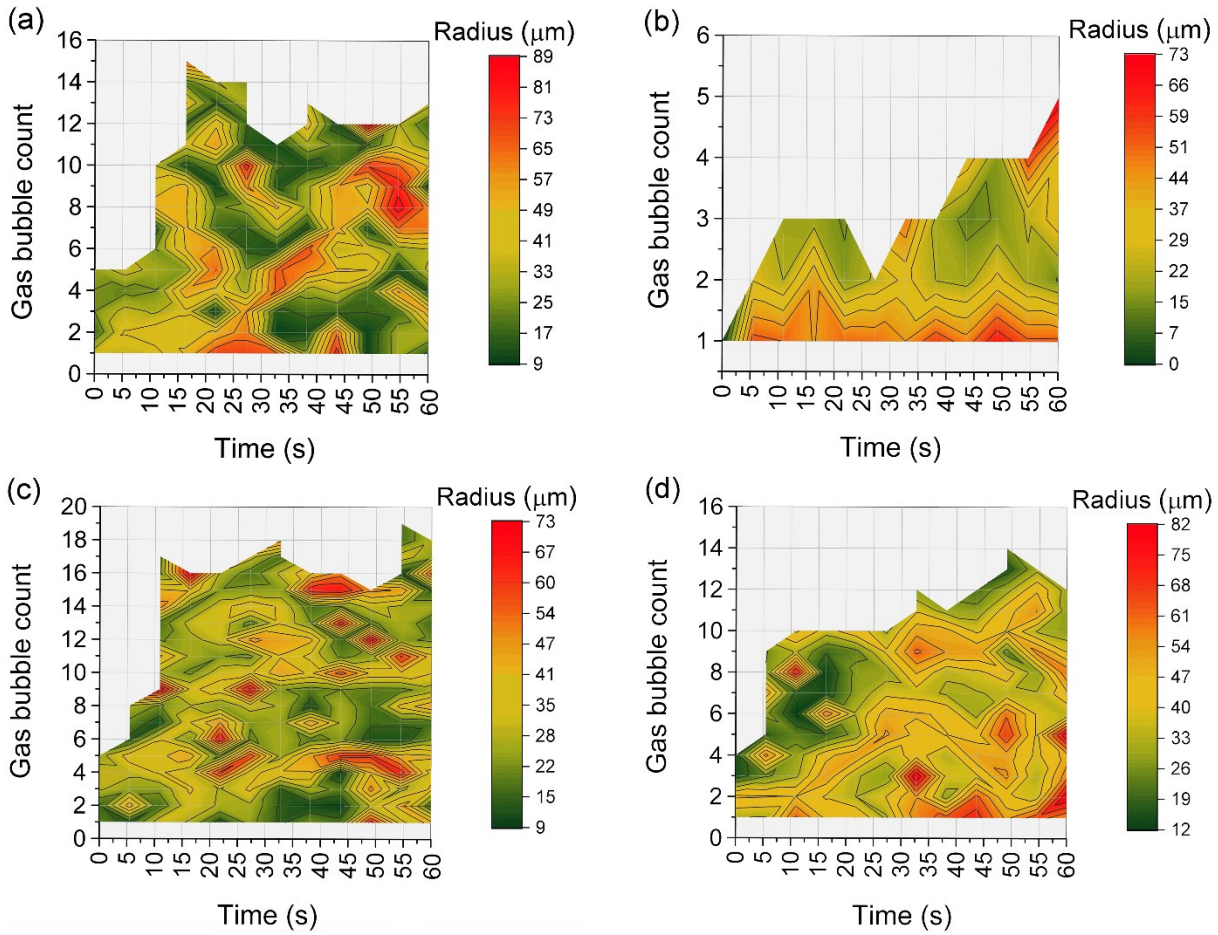

Figure S15. In situ variation of gas bubble radius with increasing HER potentials via *operando* optical microscopy during 60 s. Left: $Ni(OH)_2$@N-NiC/NF and Right: $Ni(OH)_2$/NF. Applied HER potentials: (a) and (c) 0.245 V, (b) and (d) 0.345 V (V vs RHE).

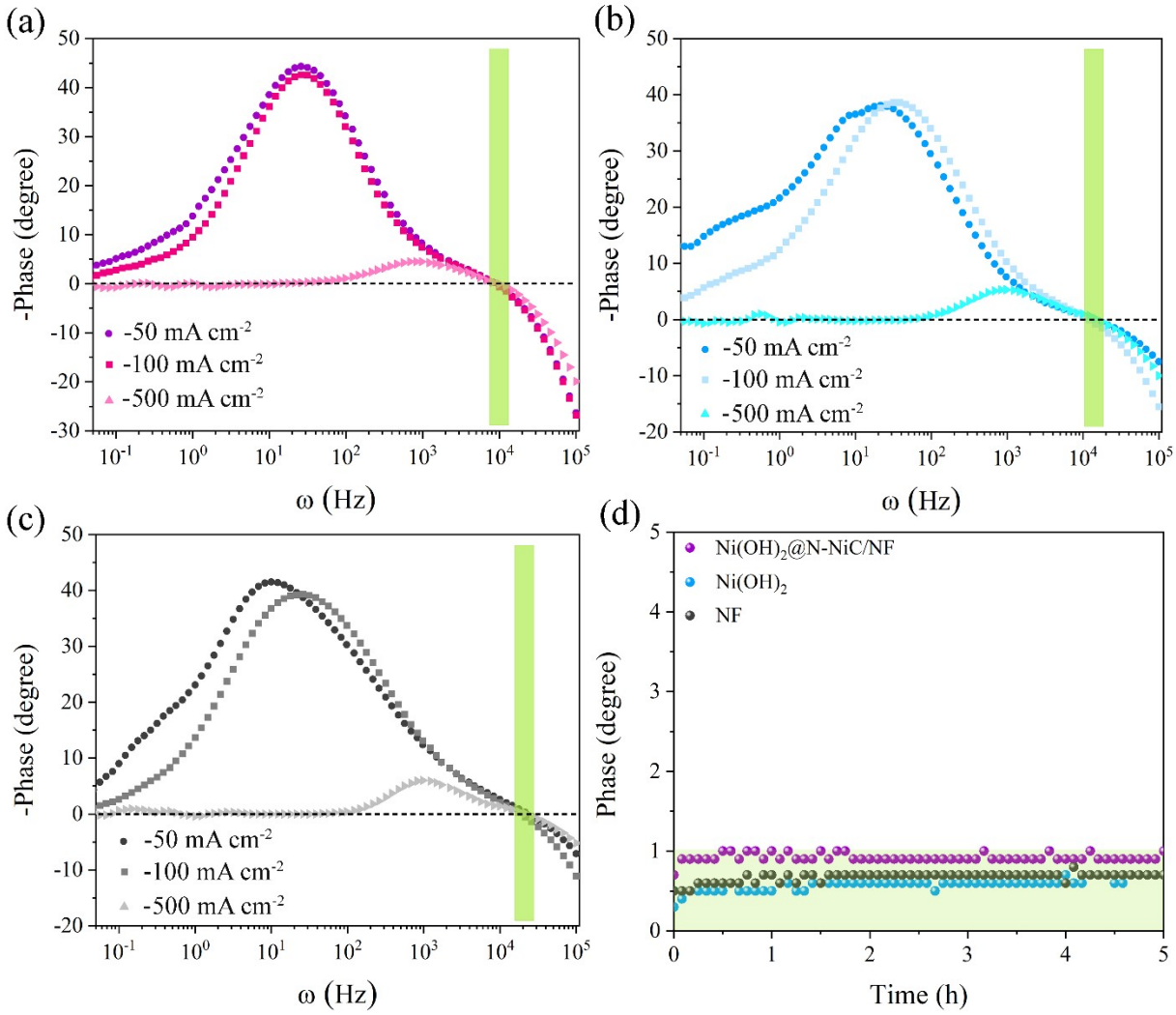

Figure S16. Bode-phase plots of (a) $Ni(OH)_2$@N-NiC/NF, (b)) $Ni(OH)_2$/NF, and (c) bare NF electrodes at different fixed current densities. (d) Dynamic phase variation for the three Ni electrodes at -100 mA cm^{-2}.

Supplementary Note 5

Bode-phase plots are acquired at various current densities to determine the frequency of the minimum phase. A frequency of around 20 kHz is opted for single frequency experiments in standard three-electrode electrochemical cell. Dynamic phase variation at this frequency shows the minimum contribution of the phase component of impedance.

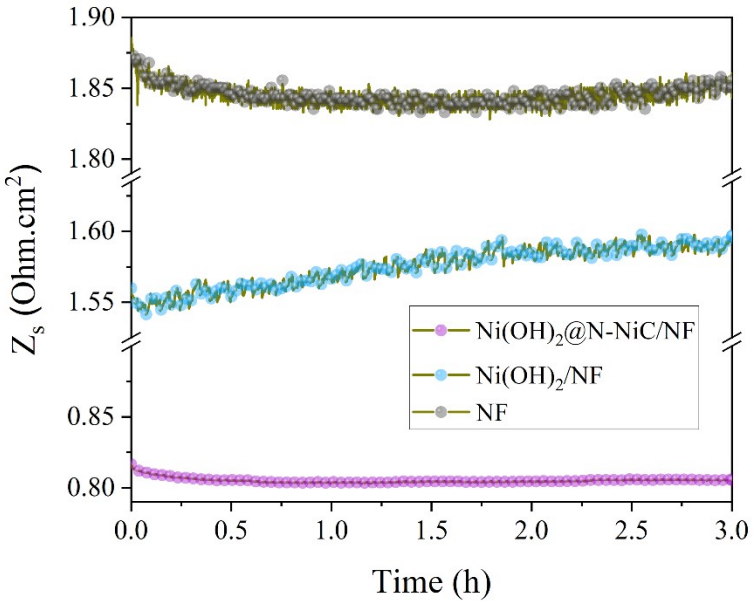

Figure S17. (a) Dynamic resistance variations of Ni(OH)$_2$@N-NiC/NF, Ni(OH)$_2$/NF, and bare NF electrodes in standard three-electrode electrochemical cell at 20 kHz and -100 mA cm^{-2} at a longer timescale.

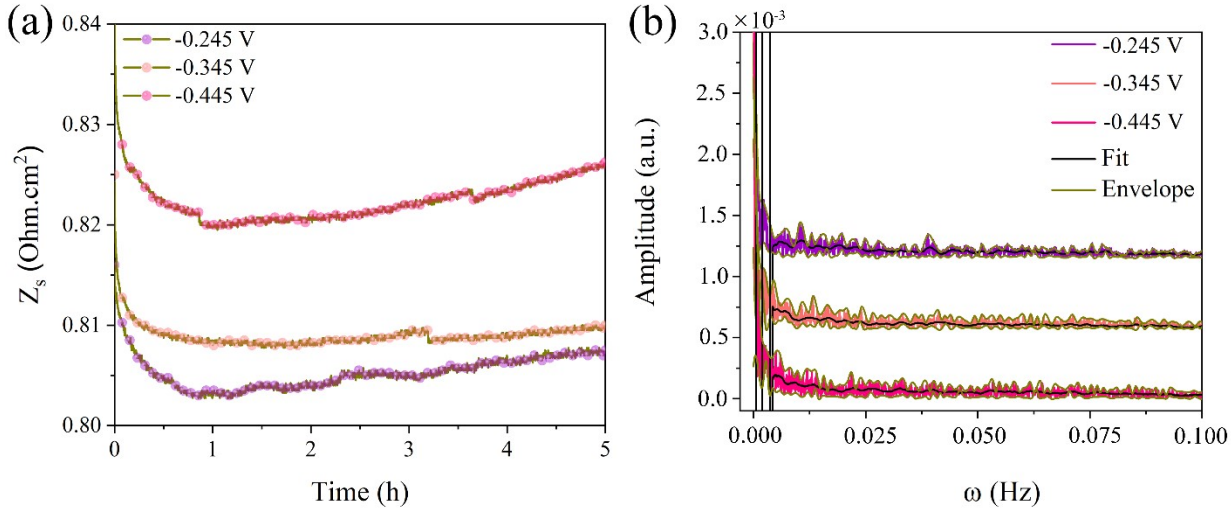

Figure S18. (a) Dynamic resistance variation of Ni(OH)$_2$@N-NiC/NF at high frequency of 20 kHz with increasing HER potential (vs RHE). (b) The corresponding FFT plots.

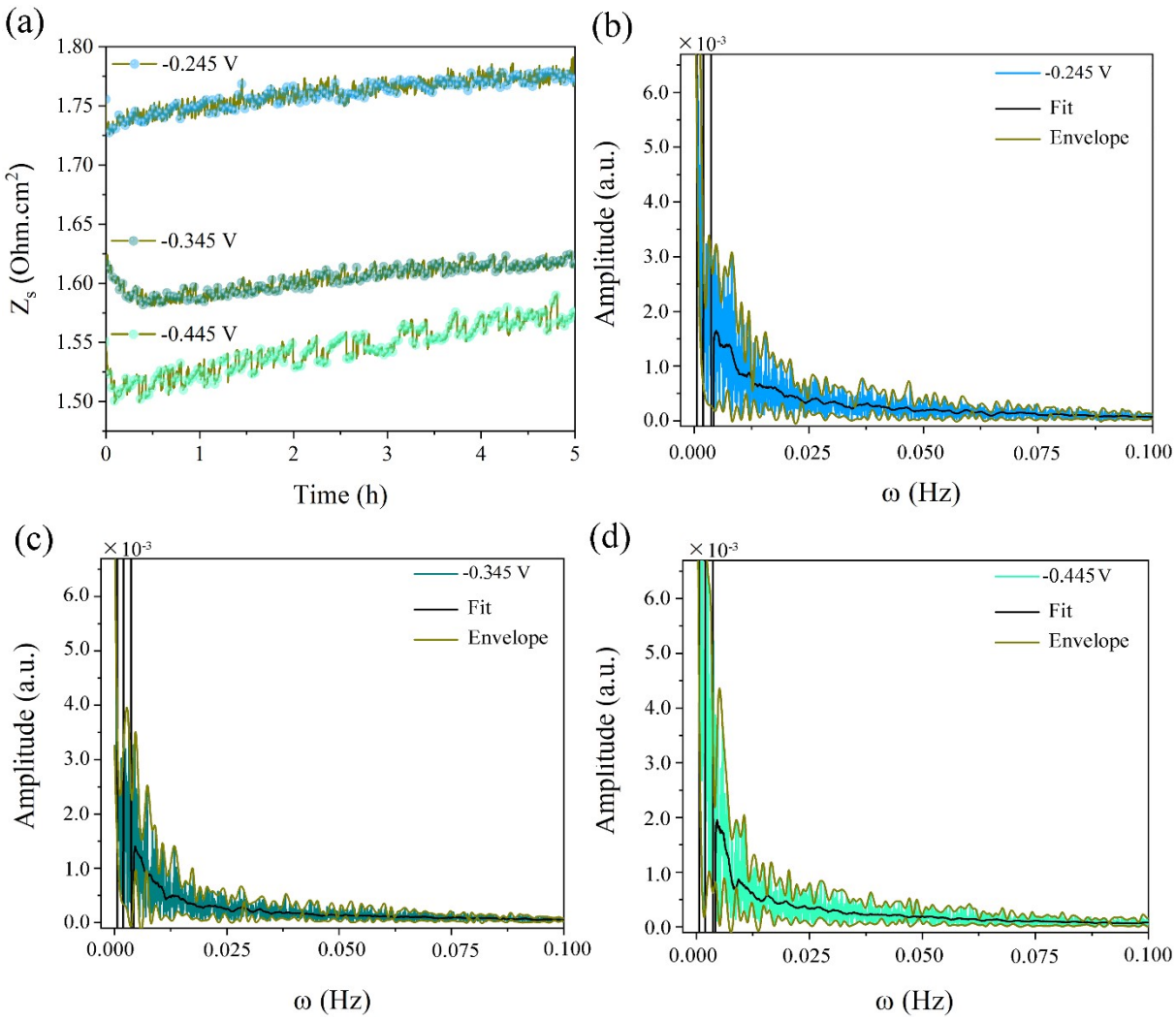

Figure S19. (a) Dynamic resistance variation of $Ni(OH)_2$/NF at high frequency of 20 kHz with increasing HER potential (vs RHE). (b) The corresponding FFT plots.

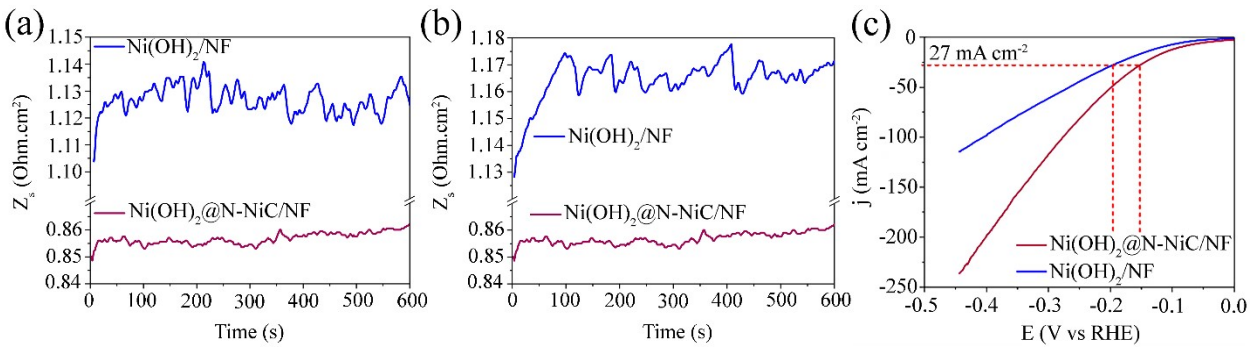

Figure S20. *Operando* dynamic resistance variation over $Ni(OH)_2$@N-NiC/NF and $Ni(OH)_2$/NF electrodes at 10 kHz at (a) -0.15 V vs RHE and (b) the equivalent potential for a constant current density of -27 mA cm^{-2}. (c) LSV curves of the two Ni electrodes in 1 M KOH.

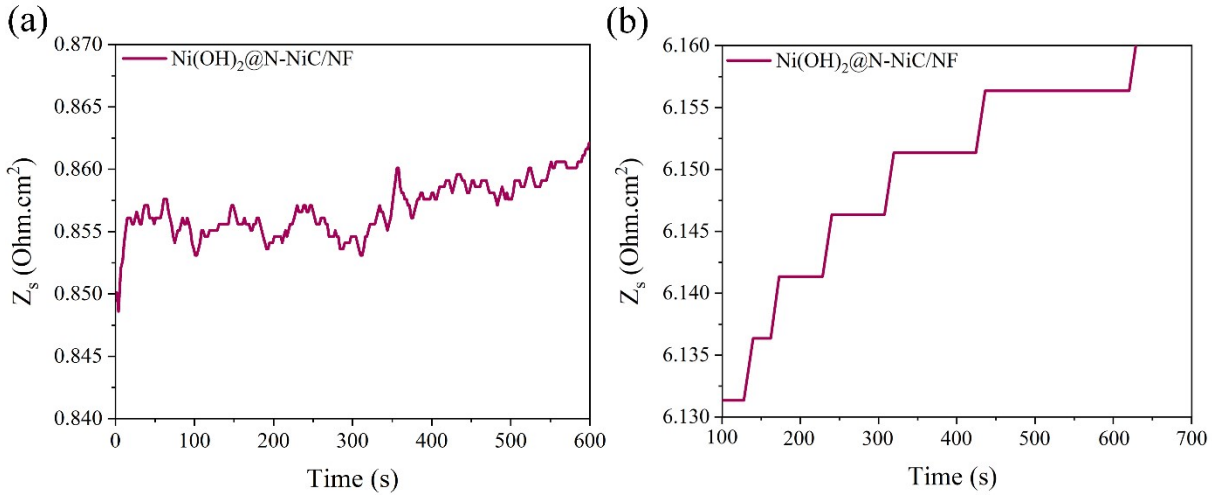

Figure S21. *Operando* dynamic resistance variation over $Ni(OH)_2$@N-NiC/NF at a HER potential of -0.15 V vs RHE at a (a) high frequency of 10 kHz and a (b) low frequency of 0.1 Hz.

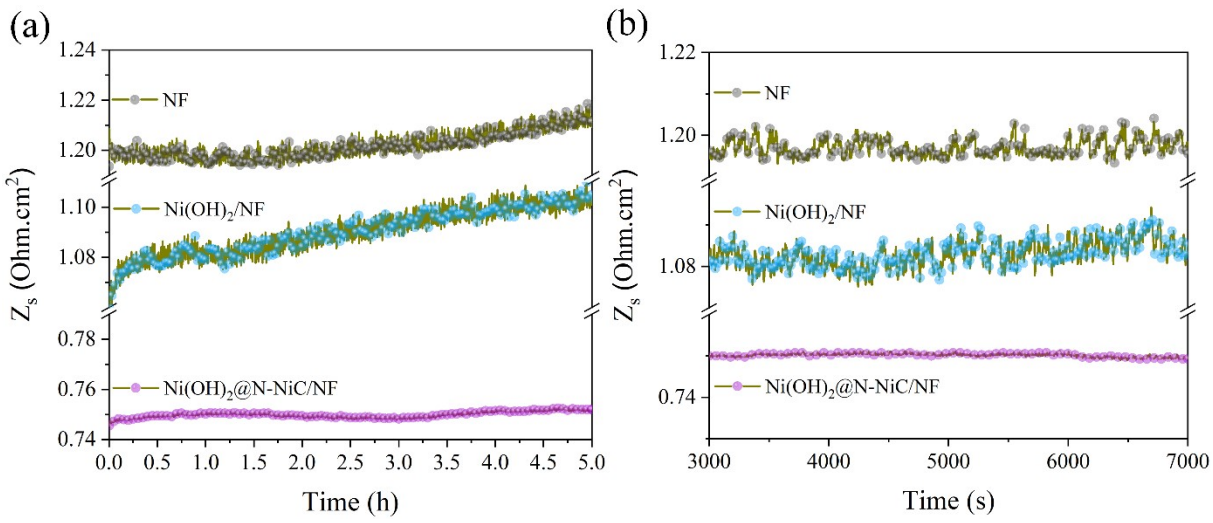

Figure S22. (a) Dynamic resistance variation at 20 kHz in standard three-electrode electrochemical cell with (b) selected time intervals for $Ni(OH)_2$@N-NiC/NF, $Ni(OH)_2$/NF, and bare NF at an OER current density of 100 mA cm^{-2}.

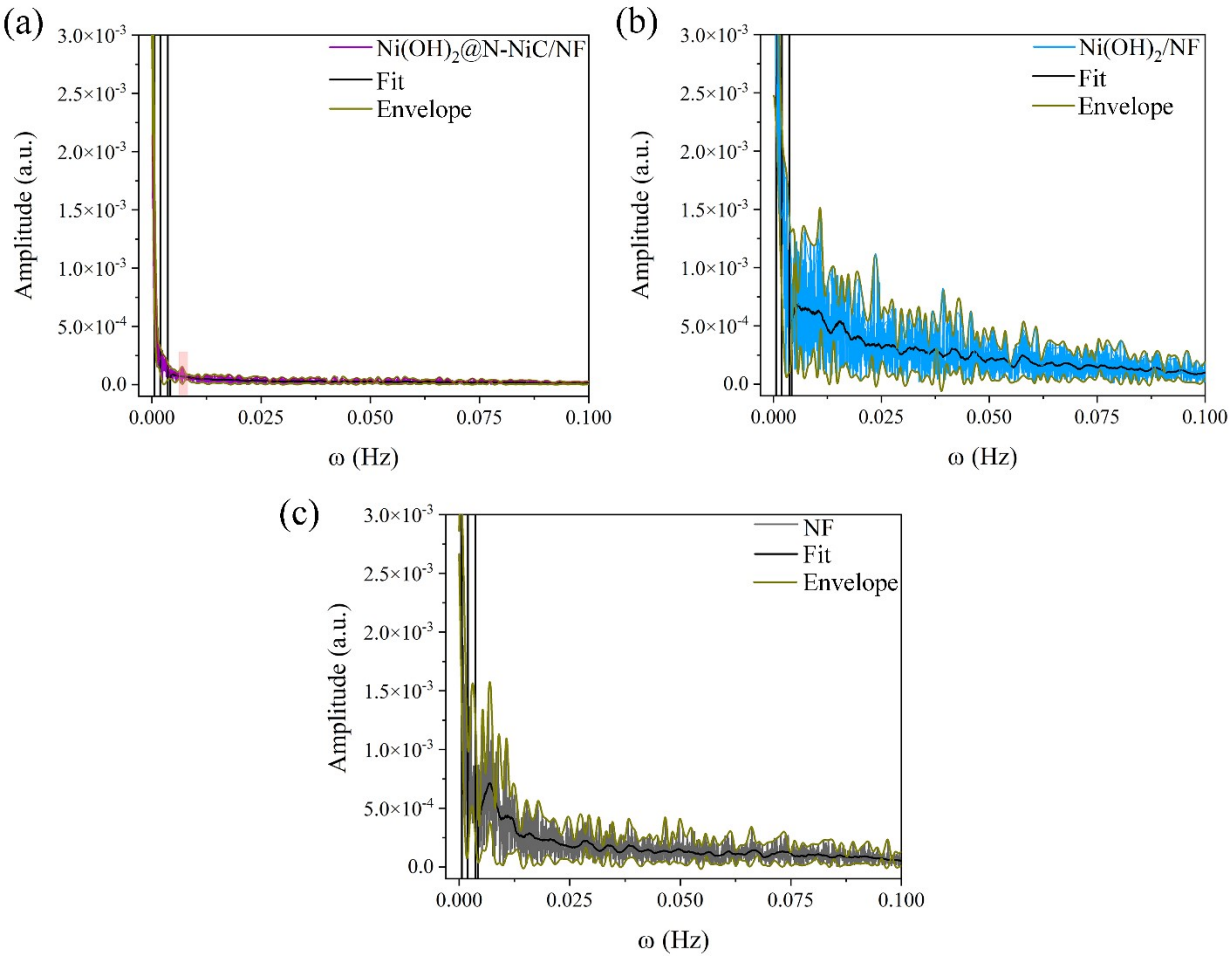

Figure S23. FFT plots of (a) $Ni(OH)_2$@N-NiC/NF, (b) $Ni(OH)_2$/NF, and (c) bare NF at an OER current density of 100 mA cm^{-2}.

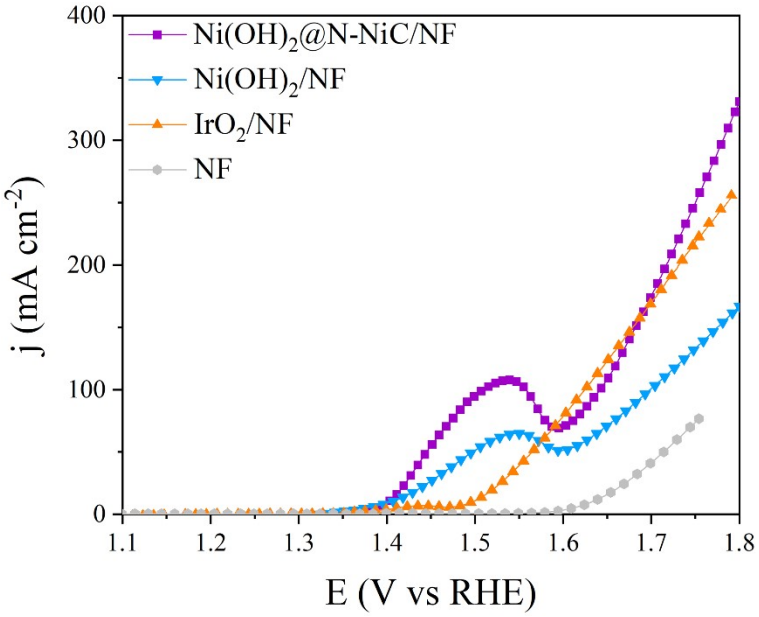

Figure S24. OER performance of $Ni(OH)_2$@N-NiC/NF compared to $Ni(OH)_2$/NF, bare NF, and benchmark IrO_2/NF in 1M KOH without ohmic resistance compensation.

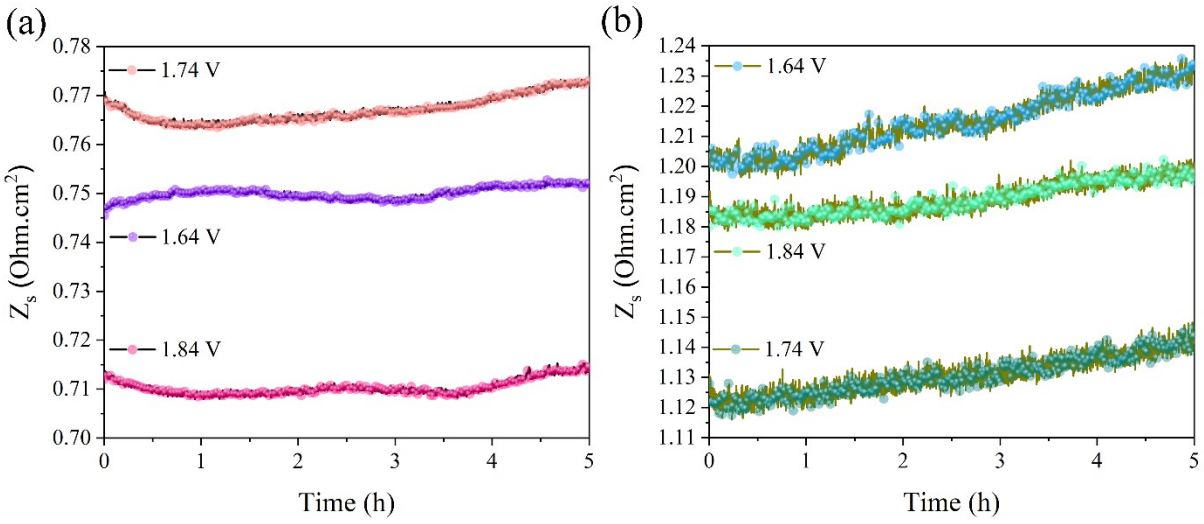

Figure S25. Dynamic resistance variations of (a) $Ni(OH)_2$@N-NiC/NF and $Ni(OH)_2$/NF in standard three-electrode electrochemical cell at 20 kHz with increasing OER potential (vs RHE).

Supplementary Note 6

Irregularities in the order of the absolute values of the recorded resistance originates from performing the EIS tests after the termination of the previous test. All in all, the difference between the absolute resistance values for OER potentials is small and does not interfere with GBE interpretation.

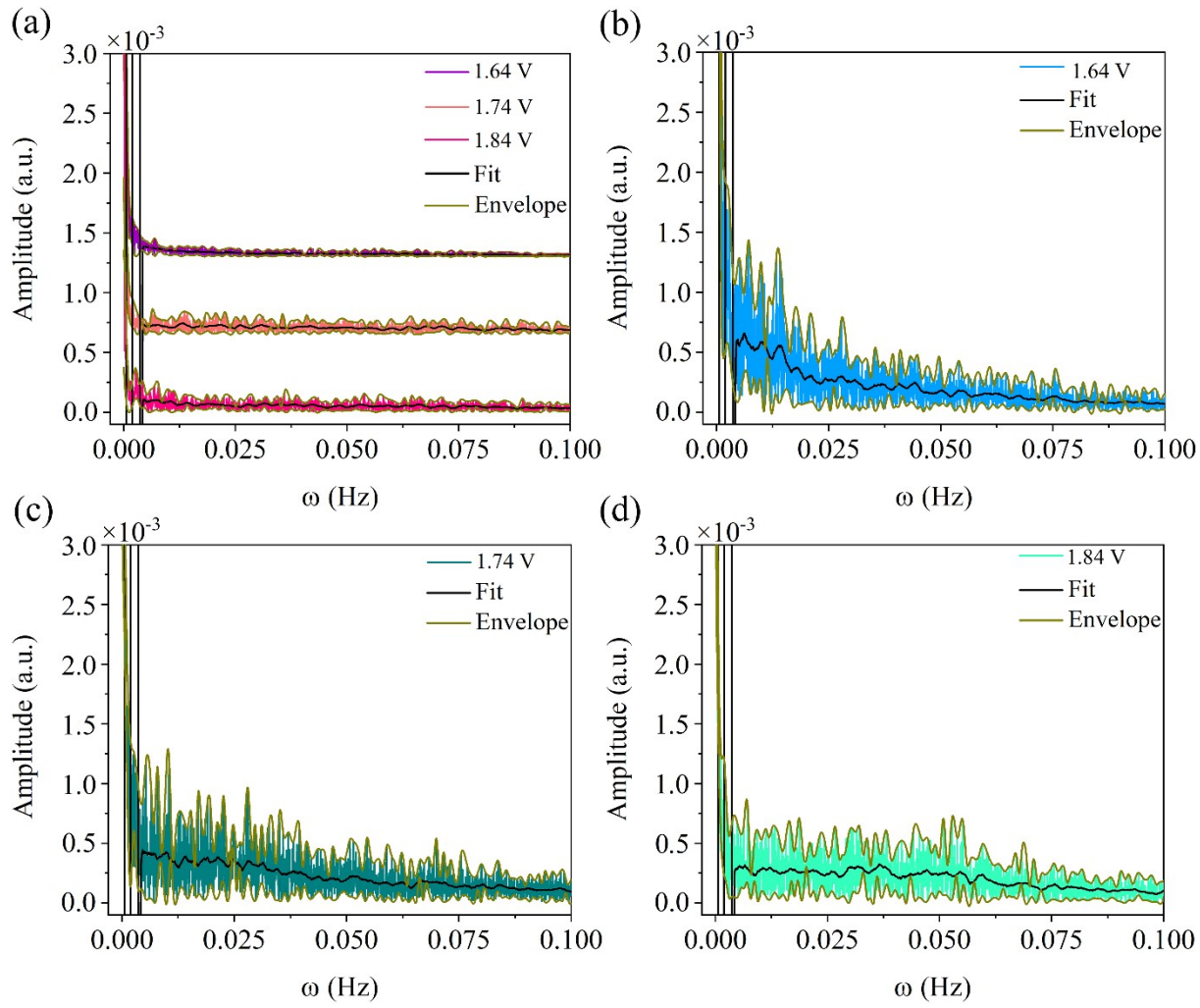

Figure S26. FFT plots at incrementing OER potentials for (a) $Ni(OH)_2$@N-NiC/NF as well as for $Ni(OH)_2$/NF at (b) 1.64 V, (c) 1.74 V, and (d) 1.84 V (V vs RHE).

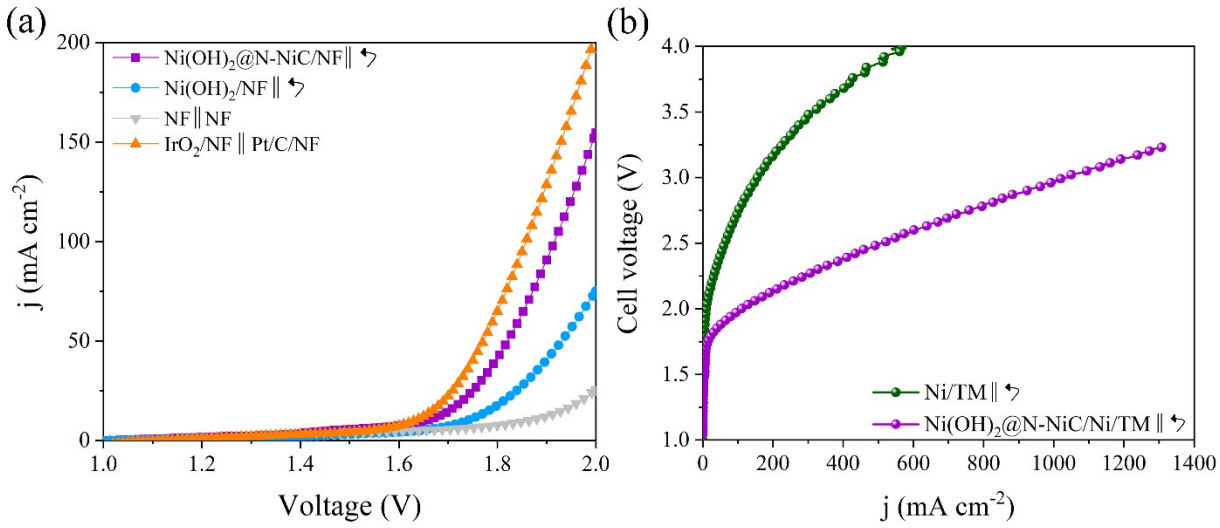

Figure S27. Water electrolysis performance at 20 °C in 1 M KOH in a (a) two-electrode alkaline water electrolyser and (b) AEM water electrolyser without ohmic drop compensation.

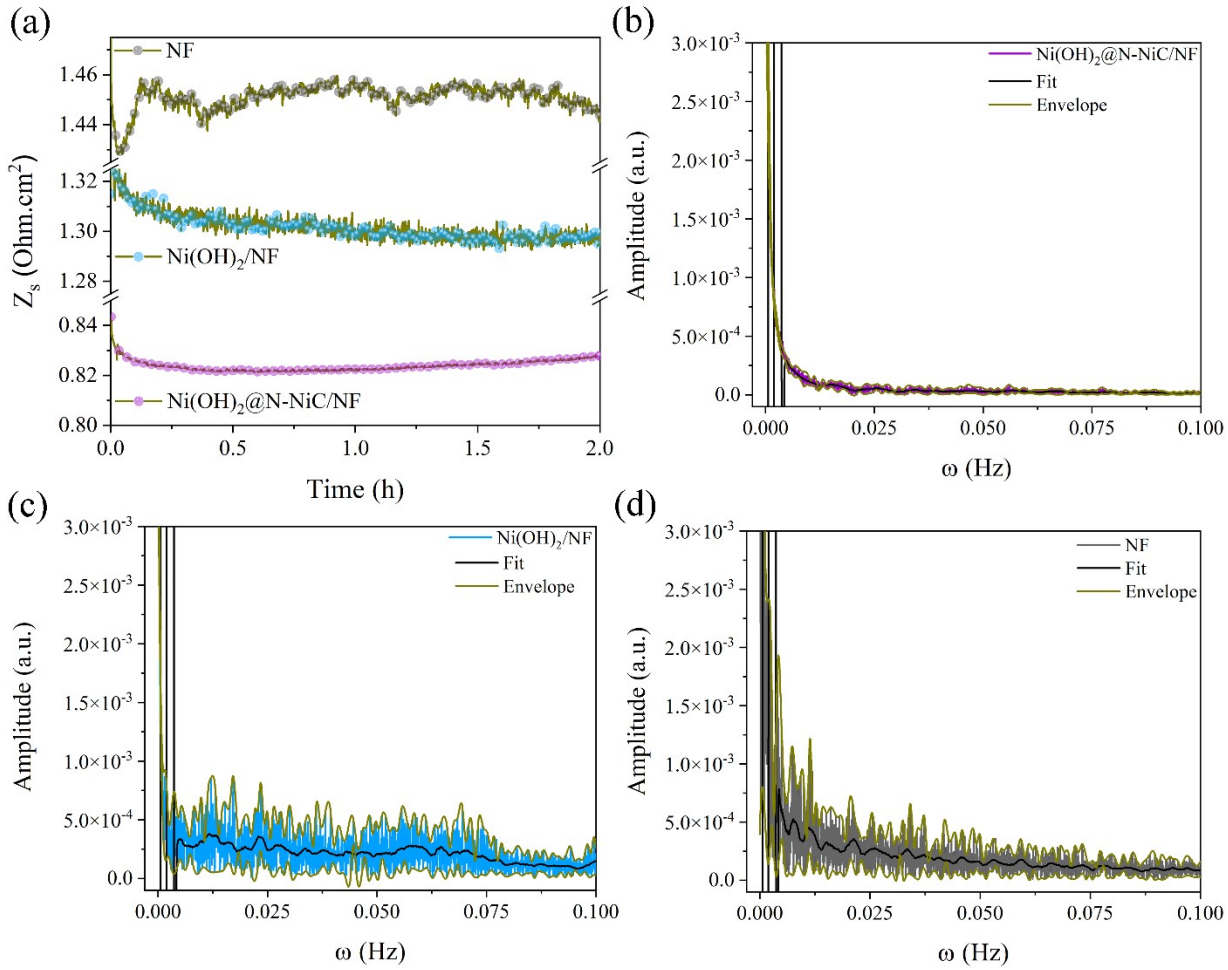

Figure S28. (a) Dynamic resistance variations of $Ni(OH)_2$@N-NiC/NF, $Ni(OH)_2$/NF, and bare NF, each used as both anode and cathode, in alkaline water electrolyser at 20 kHz and a fixed current density of 500 mA cm^{-2}. The corresponding FFT plots for (b) $Ni(OH)_2$@N-NiC/NF, (c) $Ni(OH)_2$/NF, and (d) bare NF couples.

Table S1. Input parameters used for the developed LBM model.

Description	Parameter	Values
Fluid density	$\rho 1$ and $\rho 2$	0.01 and 1.0
Gravity	F_g	2
Interaction force between fluids	F_i	Plate: 0 Sheet: 0.0002 Triangle: 0.0004

List of Supplementary Movies

Supplementary Movie 1. Operando optical microscopy recording of hydrogen gas bubble evolution over GCE at a fixed potential of -1.45 V.

Supplementary Movie 2. Operando optical microscopy recording of hydrogen gas bubble evolution over NF at a fixed potential of -0.15 V.

Supplementary Movie 3. Operando optical microscopy recording of hydrogen gas bubble evolution over $Ni(OH)_2$@N-NiC/NF at the potential of -0.15 V equivalent to a current density of -27 mA cm^{-2}.

Supplementary Movie 4. Operando optical microscopy recording of hydrogen gas bubble evolution over $Ni(OH)_2$/NF at a fixed potential of -0.15 V.

Supplementary Movie 5. Operando optical microscopy recording of hydrogen gas bubble evolution over $Ni(OH)_2$/NF at the potential of -0.195 V equivalent to a current density of -27 mA cm^{-2}.

References

1 Dastafkan, K., Meyer, Q., Chen, X. & Zhao, C. Efficient Oxygen Evolution and Gas Bubble Release Achieved by a Low Gas Bubble Adhesive Iron-Nickel Vanadate Electrocatalyst. *Small* **16**, e2002412, doi:10.1002/smll.202002412 (2020).

2 Dastafkan, K., Shen, X., Hocking, R. K., Meyer, Q. & Zhao, C. Monometallic interphasic synergy via nano-hetero-interfacing for hydrogen evolution in alkaline electrolytes. *Nat Commun* **14**, 547, doi:10.1038/s41467-023-36100-3 (2023).

3 Giacomello, A., Meloni, S., Chinappi, M. & Casciola, C. M. Cassie-Baxter and Wenzel states on a nanostructured surface: phase diagram, metastabilities, and transition mechanism by atomistic free energy calculations. *Langmuir* **28**, 10764-10772, doi:10.1021/la3018453 (2012).